metals

MDPI

Article

Characterization of Microstructure and Localized Corrosion Resistance of Heat-Treated 17-4 PH Stainless Steel Fabricated by Material Extrusion

Pietro Forcellese [1,*], Tommaso Mancia [2], Michela Simoncini [3] and Tiziano Bellezze [1,*]

[1] Department of Science and Engineering of Matter, Environment, and Urban Planning, Polytechnic University of Marche, Via Brecce Bianche, 60131 Ancona, Italy
[2] Department of Theoretical and Applied Sciences, eCampus University, Via Isimbardi, 10, 22060 Novedrate, Italy; tommaso.mancia@uniecampus.it
[3] Department of Industrial Engineering and Mathematical Science, Polytechnic University of Marche, Via Brecce Bianche, 60131 Ancona, Italy; m.simoncini@staff.univpm.it
* Correspondence: p.forcellese@staff.univpm.it (P.F.); t.bellezze@staff.univpm.it (T.B.); Tel.: +39-071-220-4413 (T.B.)

Abstract: The quality, reproducibility, and reliability of additive-manufactured parts strongly depend on optimizing printing parameters and post-processing treatments. This study evaluates the effects on the microstructure and corrosion resistance properties of solution annealing and aging heat treatments performed on 17-4 PH stainless steel samples fabricated with different build-up orientations using a material extrusion technology: the Bound Metal Deposition™. The chemical composition and microstructures were determined using X-ray diffraction, chemical etching, optical microscopy, and scanning electron microscopy. The corrosion resistance properties in neutral sodium chloride electrolytes were investigated through cyclic potentiodynamic polarization and open circuit potential monitoring and analysis. The findings demonstrated that the solution annealing heat treatment remarkably enhanced the overall corrosion resistance properties of the samples. The improvement was attributed to the growth of the ferritic phase along the grain boundaries of the martensitic matrix and a finer dispersion of copper precipitates. The aging heat treatment performed after solution annealing enhanced the ferritic phase development, resulting in a further improvement of the localized corrosion resistance properties.

Keywords: additive manufacturing; heat treatments; ferrite; copper precipitates; build-up orientations; cyclic potentiodynamic polarization; open circuit potential; corrosion resistance properties; passive film instability

check for updates

Academic Editor: Andrii Kostryzhev

Received: 30 December 2024
Revised: 22 January 2025
Accepted: 27 January 2025
Published: 29 January 2025

Citation: Forcellese, P.; Mancia, T.; Simoncini, M.; Bellezze, T. Characterization of Microstructure and Localized Corrosion Resistance of Heat-Treated 17-4 PH Stainless Steel Fabricated by Material Extrusion. *Metals* **2025**, *15*, 137. https://doi.org/10.3390/met15020137

Copyright: © 2025 by the authors. Licensee MDPI, Basel, Switzerland. This article is an open access article distributed under the terms and conditions of the Creative Commons Attribution (CC BY) license (https://creativecommons.org/licenses/by/4.0/).

1. Introduction

The corrosion resistance properties of stainless steels fabricated using additive manufacturing (AM) technologies differ from those produced with subtractive manufacturing processes. These differences can be attributed to multiple factors influencing bulk properties, including phases, porosities, and inclusions [1–5]. Depending on the chemical composition of the material, AM technique, and the printing and sintering parameters, the microstructure and the properties can change, leading to either detrimental or improved effects on the corrosion resistance properties of the stainless steel [6].

Metal AM processes are classified into seven main categories; however, the most commonly used in commercial applications are Powder Bed Fusion (PBF), Direct Energy Deposition (DED), Material Binder Jetting (MBJ), and Material Extrusion (ME) [7]. Binder

jetting and extrusion-based AM technologies share many features closely related to the powder metallurgy process of Metal Injection Molding (MIM). Therefore, the microstructural, mechanical, and corrosion resistance properties of stainless steel printed using MBJ and ME technologies are usually similar to those of MIM materials [8–10]. In principle, MIM and ME have a similar feedstock, consisting of metallic powders dispersed in a polymeric binder, which are either injected into a mold or extruded layer-by-layer onto a build plate [11,12]. In the MBJ technique, a polymeric binder is sprayed layer-by-layer onto a metallic powder bed feedstock. Thermal and solvent treatments can be used to remove most of the organic binder in the as-printed and as-extruded parts. Subsequently, a sintering process is carried out in a furnace with an inert gas atmosphere or under vacuum to eliminate the remaining polymeric binder and produce dense metallic parts [13,14].

The Bound Metal Deposition^{TM} (BMD) process, developed by Desktop Metal^{TM}, is an ME technique where a composite rod, consisting of metallic powders dispersed in a polymer wax binder, is extruded layer-by-layer onto a build plate. Studio System 2 features a printer with a 0.25 mm or 0.4 mm extruder and a sintering furnace capable of reaching temperatures up to 1400 °C. However, the samples investigated in this study were fabricated using Studio System 1, including a debinding chamber. The 17-4 PH stainless steel fabricated using the BMD achieves a density of up to 97% in inert or slightly reductive environments. The typical microstructure of an as-sintered 17-4 PH, expected to be predominantly martensitic due to the high cooling rate following the sintering process, consists of a combination of ferrite, residual austenite, and martensite grains along with printing defects, porosities, precipitates, and inclusions [12,15,16].

The corrosion resistance properties of the bulk of as-sintered 17-4 PH fabricated using BMD are lower than those of a wrought 17-4 PH [16]. This difference has been attributed to porosities left during the printing process, caused by the overlay between different layers and hatches [16]. Additionally, the presence of precipitates and inclusions, that may be formed either during sintering or the production by atomization of the metallic powders, is detrimental to the corrosion performances of this material [16].

This study examines the localized corrosion resistance properties related to the microstructure of heat-treated samples of 17-4 PH stainless steel fabricated with different build-up orientations through a Studio System (BMD). This need arose from previous studies that investigated and emphasized the importance of heat treatments on the as-sintered 17-4 PH fabricated using BMD [17], demonstrating the reduced environmental footprint of the heat-treated parts when good mechanical properties are required [18,19]. The microstructure of the BMD samples was revealed by chemical etching and examined using optical microscopy (OM), X-ray diffraction (XRD), and scanning electron microscopy with energy-dispersive X-ray analysis (SEM-EDX). Electrochemical investigations were carried out on heat-treated samples through cyclic potentiodynamic polarization (CPP) curves and open circuit potential (OCP) monitoring in neutral sodium chloride electrolytes.

2. Materials and Methods

17-4 PH stainless steel plates were fabricated by BMD technology with three different build-up orientations of 0°, 45°, and 90° concerning the build plate, as shown in Figure 1. The 17-4 PH printed plates had sides of 25 mm and a height of 3 mm. They were fabricated using a nozzle of 0.4 mm diameter, a layer thickness of 0.1 mm, and a concentric infill pattern.

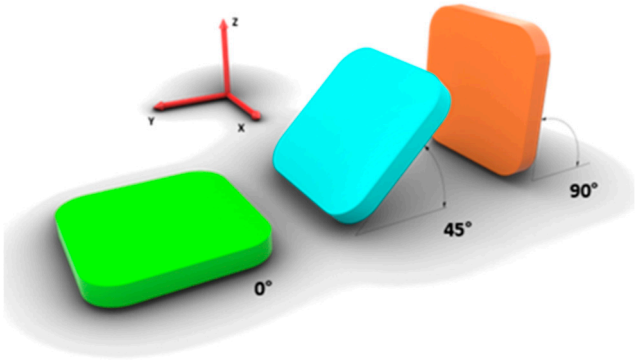

Figure 1. The schematic representation of the build-up orientations of 0°, 45°, and 90° concerning the build plate (XY plane) of the 17-4 PH samples fabricated through BMD.

The 17-4 PH samples were printed using Studio System, which includes a printer, a debinding chamber, and a sintering furnace. The as-printed plates were debound using the nonpolar organic solvent trans-1,2 dichloroethylene for 30–40 h. Afterward, the samples were sintered for up to 40 h in a slightly reductive gas atmosphere of 97% argon and 2.9% hydrogen. The thermal cycles automatically programmed by the Studio System are neither displayed nor adjustable but are designed to optimize the binder removal and sintering process.

Two post-processing heat treatments were performed on the as-sintered plates. The samples labeled as "S" underwent solution annealing for 1 h at 1040 °C and water quenching, while those labeled as "SA" underwent the same solution annealing and water quenching procedure and then aged for 1 h at 480 °C (H900).

The chemical composition of the bulk, which was ground to 1200 grit using emery paper and then cleaned by sonication in deionized water for 5 min, was analyzed at six points using a Spark Analyzer Spectrolab on the as-sintered sample fabricated by BMD with a 0° build-up orientation.

A wrought 17-4 PH, along with the as-sintered and the heat-treated samples fabricated with a 0° build-up orientation, were ground to 1200 grit using emery paper and then mirror-polished to 1 µm using spray monocrystal diamond powders. The microstructure of these samples was revealed using Kalling's etchant (1.5 g of copper chloride dissolved in 33.3 mL of water, 33.3 mL of ethanol, and 33.3 mL of hydrochloric acid) and Vilella's etchant (1 g of picric acid dissolved in 100 mL ethanol and 5 mL of hydrochloric acid). The samples were then observed with OM using an Olympus BX51 (Olympus's Optical Co., Ltd., Nagano, Japan) and SEM-EDX using a Zeiss FE-SEM SUPRA 40 (Carl Zeiss Microscopy GmbH, Jena, Germany) and a Bruker Quantax (Bruker Nano GmbH, Berlin, Germany). The SEM images and the EDX microanalysis of the microstructures revealed using Kalling's etchant were obtained using a secondary electrons detector with an applied voltage of 15 kV, an aperture size of 60 µm, and a WD of 9.4 mm.

The XRD investigation was carried out using a Bruker D8 Advance diffractometer with monochromatic Cu-Kα radiation (wavelength λ = 1.54 Å) over a 2θ range from 35° to 80°. The analysis was performed on the bulk of the wrought 17-4 PH and the as-sintered and heat-treated samples printed with a 0° build-up orientation. The samples were ground to 1200 grit using emery paper prior the XRD analysis.

The CPP and OCP electrochemical measurements were performed on S and SA heat-treated plates. The samples were embedded in a polyacrylic resin and then ground to 1200 grit using emery paper. Subsequently, the samples were cleaned by sonication in deionized water for 5 min, followed by sonication in n-hexane for 15 min, to remove any metallic powder and binder residues from the surface. A shielding polyimide tape

was applied to the surface of the samples, leaving an exposed area of 1.13 cm^2 for the electrochemical tests.

The CPP curves were recorded using a Gamry Reference 600 and Interface 1010 potentiostats (Gamry instruments, Warminster, PA, USA) in a three-electrode cell containing neutral 0.35 wt% NaCl electrolyte. The forward and reverse scan rate of the polarization curves was set to 83 $\mu V \cdot s^{-1}$, with the current density limit for reversing the scan set to 0.01 $mA \cdot cm^{-2}$. The polarization started at 15 mV below the stationary OCP, which was recorded for 30 min before the CPP tests. Electrochemical Impedance Spectroscopy (EIS) was measured before CPP in the frequency range from 100 kHz to 1 Hz, setting 10 points per decade and a signal amplitude of 10 mV for the measurements. The EIS was carried out to determine the solution resistance and correct the polarization curves for the ohmic drop. The electrochemical cell for the CPP measurements consisted of the heat-treated BMD sample as the working electrode, a Saturated Calomel Electrode (SCE, E = 0.241 V vs. SHE) as the reference electrode, and a titanium-activated wire as the counter electrode. The corrosion potential (E_{corr}), breakdown potential (E_{br}), and protection potential (E_{prot}) were evaluated for each curve. At least three polarization curves were recorded for each sample.

The OCP was monitored in a neutral 3.5 wt% NaCl electrolyte, which was ten times more concentrated in NaCl than the solution used in the CPP measurements to enhance the localized attacks on the surface of the investigated BMD samples. The corrosion potentials of the samples were recorded every 2.5 min over a 96 h exposure to the electrolyte using an SCE electrode and an Agilent Data Switching Unit (Model 34970A) equipped with a multiplexer module (Model 34901A). At least three OCP curves were recorded for each sample.

The OCP curves were analyzed between 24 h and 96 h using a numerical procedure to assess the passive film instability or its activation tendency during this time of exposure to the electrolyte. Initially, potential values corresponding to steady-state conditions (baseline points), which were not considered activation events or potential drops, were identified by applying a threshold to the derivative of the experimental corrosion potential data. A non-linear regression curve was applied to interpolate the baseline points, enabling the identification of potential drops exceeding a −10 mV threshold relative to the baseline. These drops were considered activation events of the passive film and were evaluated using a routine implemented in Excel VBA. The algorithm calculated the areas of each drop, expressed in [V·h], by integration using the trapezoidal rule. The sum of the areas of the potential drops calculated between 24 h and 96 h for each sample was considered as an index of the passive film instability during the exposure to the neutral sodium chloride electrolyte [16,17].

3. Results and Discussion

The average chemical composition of the bulk of the as-sintered 17-4 PH fabricated through BMD is reported in Table 1. The values were similar to those found in other studies and fell within the range given by the Desktop Metal technical datasheet [16]. The chemical composition of the as-sintered bulk is representative of a 17-4 PH; moreover, the silicon content was lower than in the previous study [16], most likely because that analysis was conducted on an as-built sample without grinding and cleaning the surface, thus representing the external layer in place of the bulk considered in this study.

Table 1. Average chemical composition (wt.%) of the as-sintered (BMD) bulk.

Cr	Ni	Cu	Si	C	Mn	Mo	Fe
15.82	4.64	3.48	0.79	0.01	0.54	0.11	Bal.

The microstructures of the wrought 17-4 PH and the as-sintered and heat-treated samples (0° build-up orientation) revealed using Kalling's etchant are shown in Figure 2. The 45° and 90° samples are not included here, as no significant differences were observed among the different build-up orientations. The abundance of porosity, defects, oxides, and inclusions observed using the OM technique indicates a complex bulk microstructure, consistent with other studies on 17-4 PH samples fabricated by BMD [15,16,20].

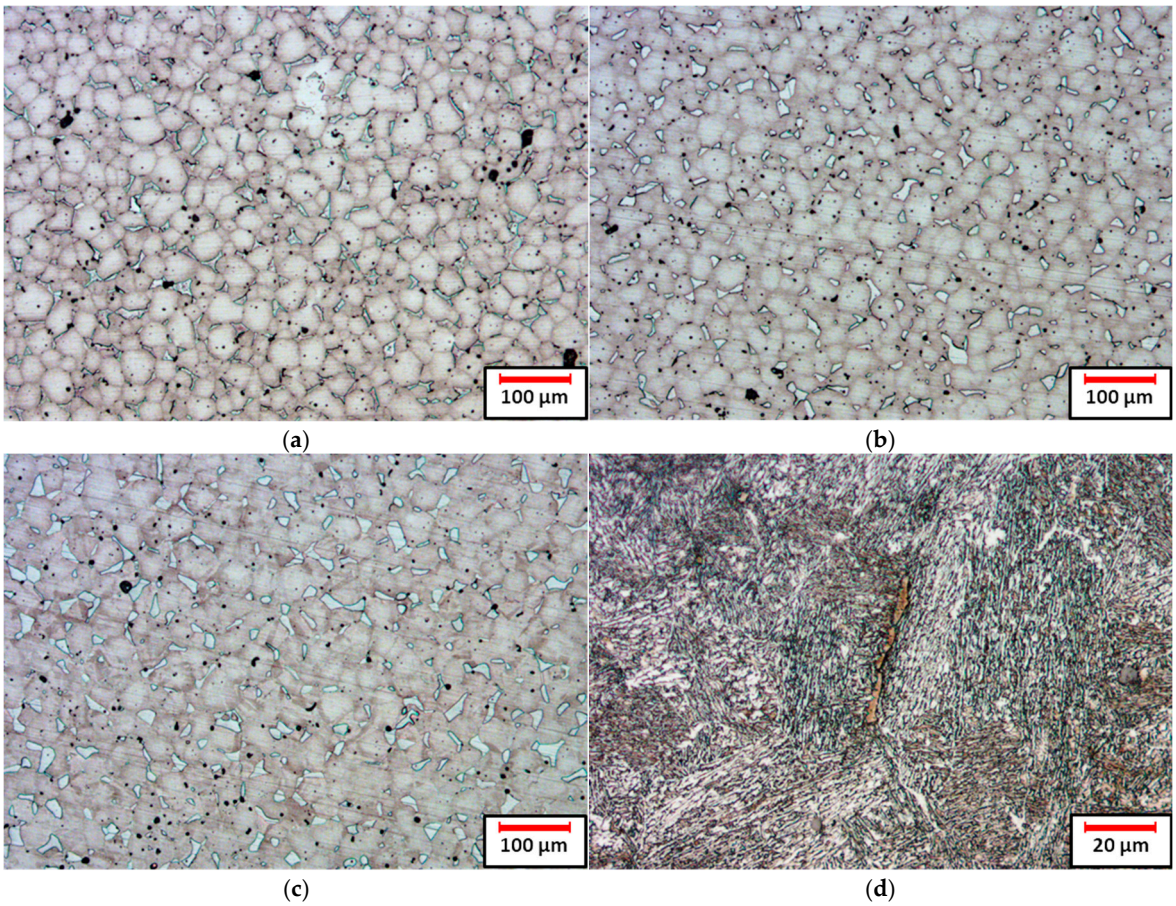

(**a**) (**b**) (**c**) (**d**)

Figure 2. OM observations of the microstructures revealed using Kalling's etchant of wrought 17-4 PH and BMD samples with a 0° build-up orientation: as-sintered (**a**), S (**b**), and SA (**c**). The magnification required to observe the microstructure of the wrought 17-4 PH (**d**) was five times higher.

Although the typical martensitic microstructure is not visible in the as-sintered sample (Figure 2a), other authors have reported that the grains revealed by chemical etching on BMD, MBJ, and MIM samples are mostly martensite, which is known to appear dark when Kalling's etchant is used [15,21–23]. Some authors have reported the formation of a small fraction of ferrite and residual austenite at the martensitic grain boundaries during the sintering process, attributed to the diffusion of residual carbon from the residual polymeric binder in the matrix [12,15,21,22]. The formation of δ-ferrite is typical of sintered stainless steel, particularly for MBJ, and can be attributed to the fast cooling rates at sintering temperatures above 1394 °C [24–28].

It is unclear whether the brighter phase at the boundaries of the martensitic grains (dark phase) is austenitic or ferritic. At higher magnifications, this bright phase appears intermediate, with lighter regions that shall correspond to austenite and colored areas to ferrite when Kalling's etchant is used, despite other studies reporting the presence of only δ-ferrite along with martensite [12,15,29–32].

The microstructure changed after solution annealing (Figure 2b), resulting in an increased fraction of the bright grains at the martensitic matrix boundaries, compared to the as-sintered sample shown in Figure 2a. In this case, the bright grains appear lighter than the as-sintered, suggesting the presence of residual austenite. In other studies, the formation of up to 38% volume fraction of austenite after solution annealing at 1050 °C for 1 h has been reported in the bulk of 17-4 PH samples fabricated using MBJ technology [23].

Figure 2c shows that the bright grains fraction of the SA sample has slightly increased compared to the S sample (Figure 2b). The H900 aging heat treatment performed on wrought 17-4 PH enhances the kinetics of austenite formation due to the diffusion and precipitation of alloying elements, such as copper, which appears bright when Kalling's etchant is used [23].

The microstructure of the wrought 17-4 PH (Figure 2d) required a magnification five times higher than that of the other samples, revealing a finer grain structure than the as-sintered and heat-treated BMD samples (Figure 2a–c). The typical microstructure of 17-4 PH, shown in Figure 2d, consists of a fully martensitic matrix (dark phase), a residual austenitic fraction (bright phase), and a few δ-ferrite stringers (colored phase). This demonstrates that the microstructure of the BMD samples is fundamentally different from that of the wrought and that it cannot be achieved even after solution annealing and aging heat treatments at typical temperatures for conventional manufacturing processes.

Although prior OM observations on the microstructure (Figure 2) and the literature suggested the presence of an austenitic phase in the as-sintered and heat-treated BMD samples [21,23], the XRD diffractograms shown in Figure 3 indicate the only presence of the BCC phase. On the other hand, the characteristic peaks associated with residual austenite (FCC) have been detected in the wrought 17-4 PH sample.

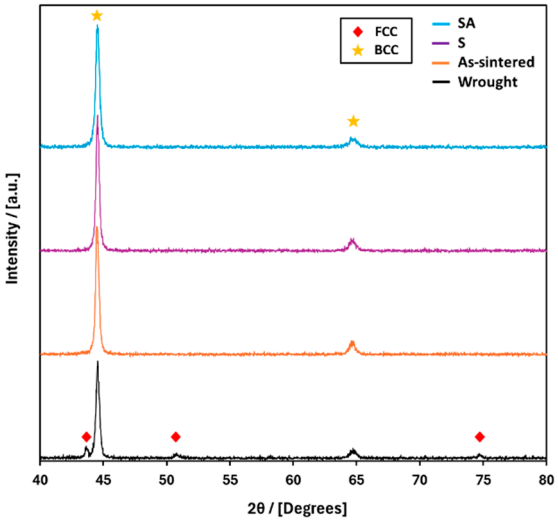

Figure 3. XRD diffractograms of the bulk for wrought 17-4 PH and as-sintered and the heat-treated samples printed by BMD with a 0° build-up orientation. The FCC (residual austenite) and BCC peaks are labeled.

The absence of residual austenite (FCC) in the heat-treated BMD samples may be explained by the fast cooling rates of the solution annealing due to the water quenching and a low aging temperature [33].

Oxides, carbides, precipitates, and inclusions were revealed using Vilella's etchant on as-sintered and heat-treated 0° samples (Figure 4), although they could not be distinguished and thus identified using OM. These were found abundant at the grain boundaries between the martensitic matrix and the bright grain of the as-sintered sample (Figure 4a). On the other hand, they were almost absent in the S sample (Figure 4b) and not observed in the

SA sample (Figure 2c). The 45° and 90° build-up orientations are not included here, as no significant differences were observed among the different build-up orientations.

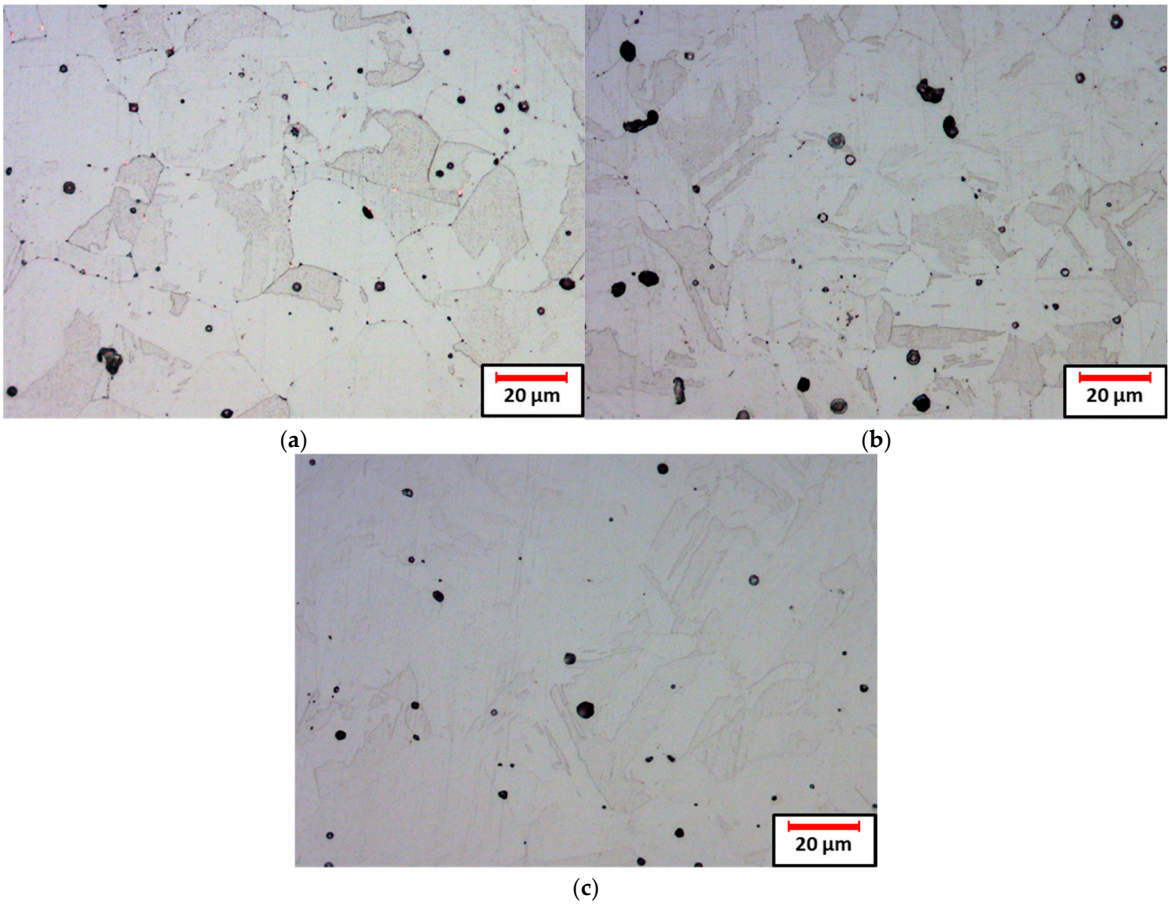

(**a**) (**b**)

(**c**)

Figure 4. OM observations of the microstructures revealed using Vilella's etchant of wrought 17-4 PH and BMD samples with a 0° build-up orientation: as-sintered (**a**), S (**b**), and SA (**c**).

The SEM-EDX investigation shown in Figure 5 was conducted on the microstructures revealed with Kalling's etchant of the 0° as-sintered and heat-treated BMD samples (Figure 2), to characterize the morphology and the chemical composition of grains, inclusions, oxides, carbides, and precipitates observed in Figures 2 and 4.

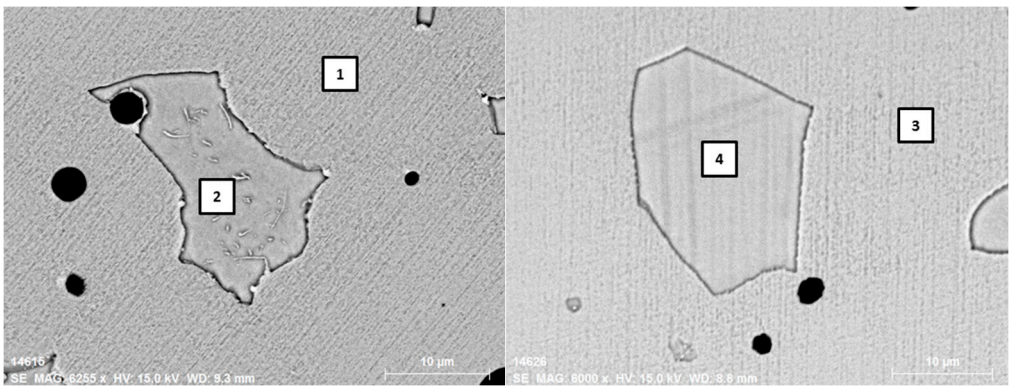

(**a**) (**b**)

Figure 5. *Cont.*

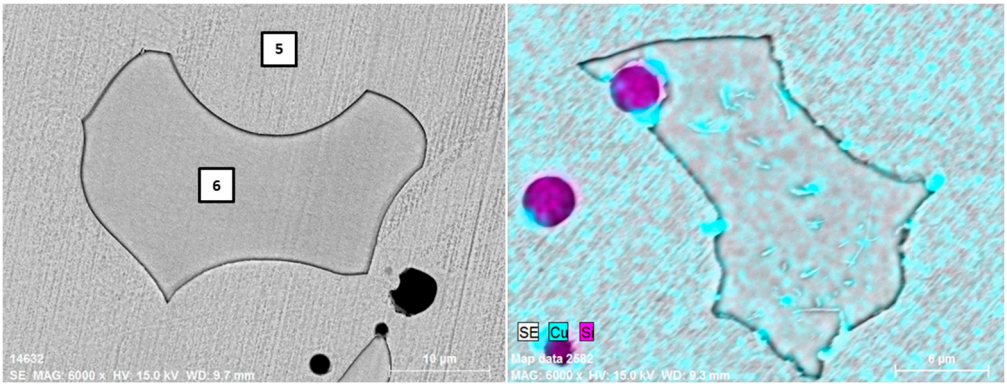

(**c**) (**d**)

Figure 5. SEM-EDX analysis of the microstructures revealed using Kalling's etchant of as-sintered and heat-treated 0° samples: as-sintered (**a**), S (**b**), and SA (**c**). The numbers indicate the sampling points of the EDX analysis. Copper and silicon in the as-sintered sample were mapped using EDX and overlaid on the secondary electron detector image (**d**).

The morphology of the bright grains, observed in the as-sintered and heat-treated samples in Figure 2 and corresponding to the sampling points 2, 4, and 6 (shown in Figure 5a, 5b, and 5c, respectively), appeared more etched compared to the martensitic matrix corresponding to the sampling points 1, 3, and 5. The chemical composition reported in Table 2 and the pronounced etching of the bright grains suggest that this phase is ferritic. Although bright grains revealed using Kalling's etchant typically represent an austenitic phase and colored grains the ferritic phase, as seen in the wrought 17-4 PH in Figure 2d.

Table 2. Chemical composition (wt.%) obtained through EDX analysis of the sampling points shown in Figure 5.

Sampling Point	Cr	Ni	Cu	Si	Fe
1 (as-sintered, martensitic matrix)	15.90	4.33	3.98	0.52	75.27
2 (as-sintered, bright grain)	22.14	1.93	1.22	0.67	74.04
3 (S, martensitic matrix)	16.19	3.93	4.47	0.49	74.92
4 (S, bright grain)	21.70	2.03	1.98	0.93	73.36
5 (SA, martensitic matrix)	15.47	4.37	5.43	0.66	74.07
6 (SA, bright grain)	20.66	2.41	2.66	0.71	73.56

The chemical composition of the ferritic grains (bright grains) of the BMD samples (sampling points 2, 4, and 6 of Figure 5) is far from the typical 17-4 PH since they are characterized by enrichment in chromium (approximately 21–22 wt.%), which is a ferrite-stabilizing element, and low nickel and copper content. On the other hand, the chemical composition of the martensitic matrix, the most abundant and dark phase shown in Figure 2, is close to that measured through the spark analyzer (Table 1), particularly for chromium and nickel, even though the copper content is approximately 1–2 wt.% higher than expected.

The SEM-EDX elements map (Figure 5d) also revealed the presence of silicon oxide inclusions, consistent with the black spots of the etched surfaces of the BMD samples observed using OM (Figures 2 and 4). The silicon inclusions are a typical feature of the bulk of the 17-4 PH fabricated through BMD, agreeing with findings from other studies [16,20,31,32,34]. Along with the silicon oxides, numerous copper precipitates have also been found in the as-sintered sample (Figure 5d), mostly at the interface between the martensitic matrix and the ferritic phase, consistent with the OM images in Figure 4a. The copper map in Figure 5d suggests that the size of the copper precipitates is larger than

expected, measuring a few hundred rather than tens of nanometers. Similar findings have been reported in the literature for 17-4 PH fabricated using ME technologies [30,31]. This may be explained by the formation of clusters of precipitates so close to each other that the SEM-EDX setup is inadequate for the characterization at nanometer scales. Furthermore, investigating the morphology of copper precipitates using a secondary electron detector was challenging, as many were found beneath the metallic surface. Copper precipitates were not detected at micrometer scales in the SEM-EDX investigations of the heat-treated samples. This observation corroborates the OM images shown in Figure 4b,c, which revealed the absence of oxides, carbides, precipitates, and inclusions at the grain boundaries following the heat treatments, further suggesting a homogeneous distribution of the copper precipitates. A finer dispersion in the heat-treated samples is also supported by an increase of approximately 1 wt.% in the copper content of the martensitic matrix and the ferritic phase observed in the EDX analysis (Table 2).

Figure 6 shows the most representative CPP curves in a neutral sodium chloride environment of the BMD samples with a build-up orientation of 0°, 45°, and 90° and heat-treated by solution annealing. The forward scan (anodic trait) of the curves is characterized by passive behavior with many metastable pitting events, typical of a wrought 17-4 PH and in contrast with the as-sintered samples investigated in other studies [16].

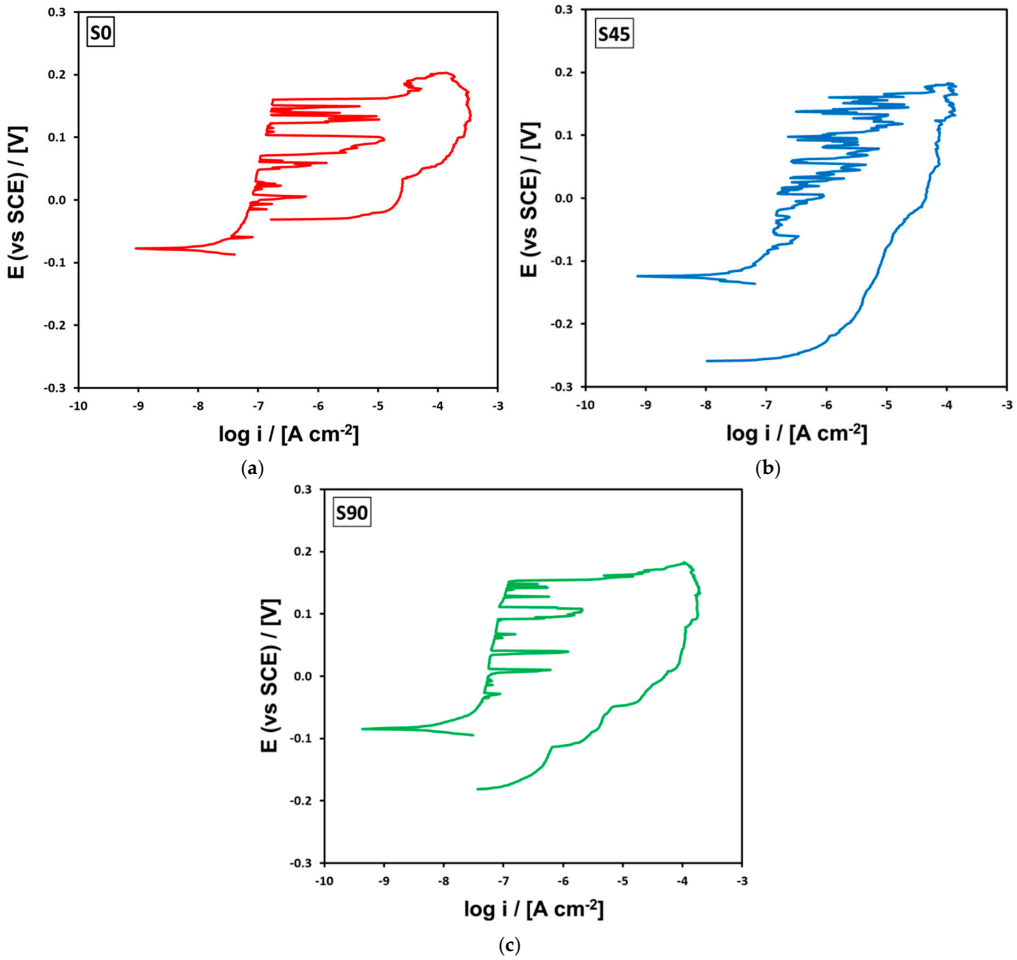

Figure 6. Most representative CPP curves recorded in a neutral 0.35 wt% NaCl electrolyte for samples printed with different build-up orientations and heat-treated by solution annealing: S0 (**a**), S45 (**b**), and S90 (**c**).

The change in the microstructure observed in the solution-annealed samples in Figures 2b and 4b plays a key role in the localized corrosion resistance properties. The CPP

curves of as-sintered samples fabricated by BMD with the same printing setup investigated in this study were characterized in other research by an active-like behavior [16]. These as-sintered samples did not exhibit passive traits and a distinct E_{br}, in contrast with the solution-annealed samples (Figure 6). The growth of the ferritic phase after solution annealing (bright grains in Figure 2b) enhanced the passive film corrosion resistance properties due to the higher chromium content than the martensitic matrix (Figure 5 and Table 2), which corresponds to a greater electrochemical nobility in neutral sodium chloride environment. Additionally, this enhancement can be attributed to the finer distribution of copper precipitates following the heat treatment, which reduces the localized corrosion sites (Figure 4b) [35,36]. The solution-annealed samples showed pitting and crevice corrosion attacks after the CPP tests, whereas the as-sintered samples with the same build-up orientations showed only crevices [16].

The corrosion resistance properties of the solution-annealed samples, particularly S0, are similar to those of a wrought 17-4 PH in neutral sodium chloride electrolytes showing perfect passivity, which is typically characterized by many metastable pitting events occurring in the passive trait of the curve [16]. The S45 samples showed imperfect passivity and, in some cases, the passive trait was limitedly evident, indicating worse corrosion resistance properties than the other solution-annealed samples.

The CPP curves of the solution-annealed and then aged (H900) samples, shown in Figure 7, exhibited anodic passive behavior with many metastable pitting events, similar to the curves of the solution-annealed samples (Figure 6).

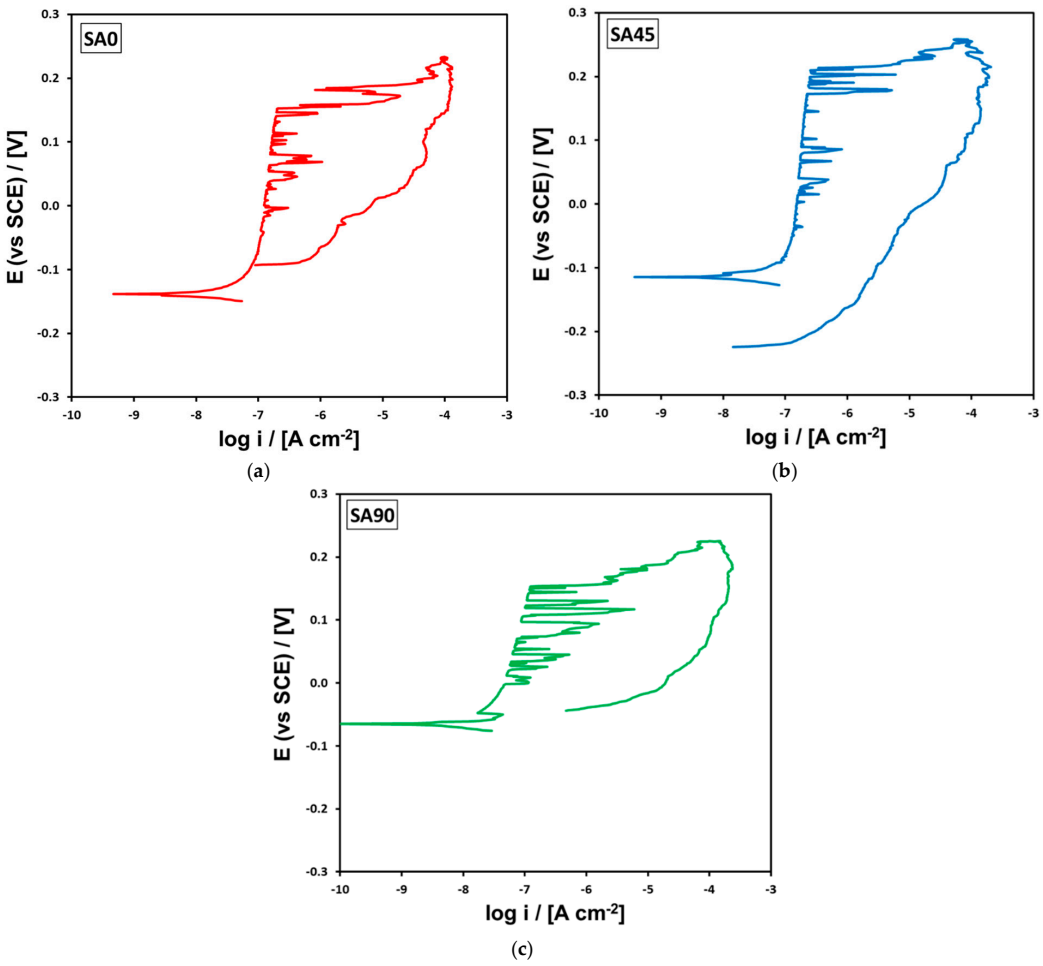

Figure 7. Most representative CPP curves recorded in a neutral 0.35 wt% NaCl electrolyte for samples printed with different build-up orientations and heat-treated by solution annealing and then aged (H900): SA0 (**a**), SA45 (**b**), and SA90 (**c**).

Although the S and SA curves appear similar in shape and characteristic potentials, fewer metastable pitting events were observed in the curves of the aged samples, particularly in the SA45 where a clear passive trait is now evident, unlike for the S45 samples shown in Figure 6b. The SA samples showed pitting and crevice corrosion attacks after the CPP tests, as well as S samples. The enhancement of the corrosion resistance properties after the aging heat treatment can be attributed to the growth of the ferritic phase at the grain boundaries of the martensitic matrix shown in Figure 2c.

The average values and standard deviations of the characteristic potentials (E_{corr}, E_{br}, and E_{prot}) obtained from the CPP curves of the heat-treated samples are plotted in Figure 8.

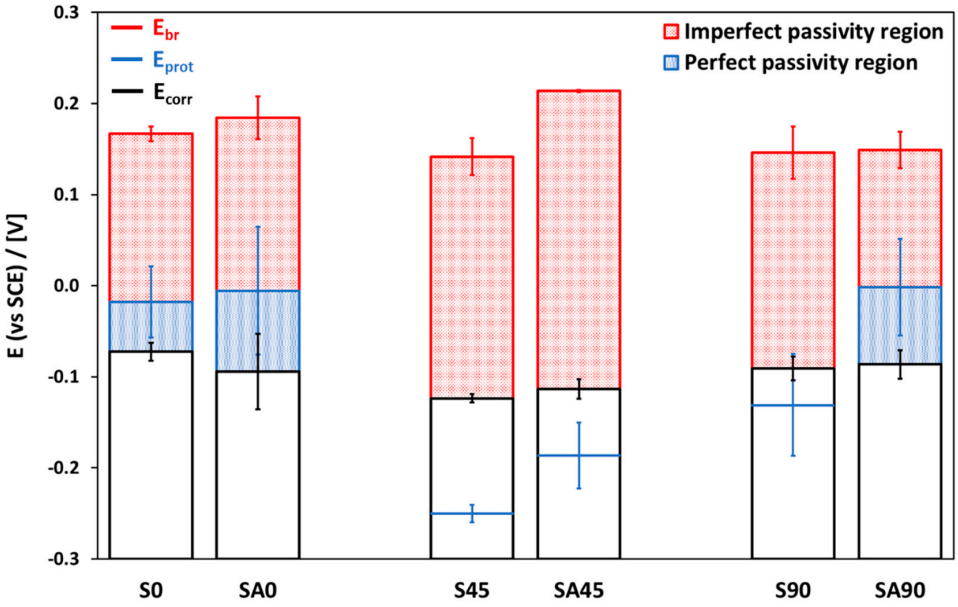

Figure 8. Average values and standard deviations of the characteristic potentials (E_{br}, E_{prot}, and E_{corr}) of the BMD samples obtained from the CPP curves recorded in a neutral 0.35 wt% NaCl electrolyte. Imperfect (red area) and perfect (blue area) passivity regions of the curves have been highlighted.

The heat-treated 0° samples (S0 and SA0) exhibited the best performance in terms of localized corrosion resistance properties, as a distinct perfect passivity region ($E_{prot} > E_{corr}$) was observed in each CPP curve (Figures 6a, 7, and 8) and E_{br} values were close to those of a wrought 17-4 PH [16]. No significant differences were observed in the 0° build-up orientation after the H900 heat treatment, aside from a slight increase in E_{br}. On the other hand, the 45° and 90° samples exhibited improved localized corrosion resistance properties following the aging process. The average values of E_{br} and E_{rep} in the SA45 samples increased by 72 mV and 64 mV, respectively, compared to the S45 samples. However, this increase was insufficient to achieve perfect passivity (Figure 8). The E_{br} of the SA90 samples increased by 129 mV compared to the S90, resulting in a transition from imperfect passivity to perfect passivity, although the E_{br} was equivalent to that of the solution-annealed samples.

The differences in the localized corrosion resistance properties among the three build-up orientations, particularly for the solution-annealed samples, can be explained by the presence of porosities (or printing defects) in the bulk of the stainless steel, produced during the layer-by-layer extrusion of the composite rod [15,16,20]. It is also important to highlight that these bulk printing defects are heterogeneous, which can also explain the standard deviations of the average values of the characteristic potentials (E_{br}, E_{prot}, and E_{corr}) shown in Figure 8, as well as the reproducibility of the CPP curves shown in Figures 6 and 7. It is well known that the presence of porosities on the investigated surface of additive-manufactured stainless steel reduces the overall corrosion resistance properties,

leading to an increased occurrence of metastable pitting events in the anodic trait and a decrease in E_{rep} [1,6,16,17]. According to other studies [16,20], these printing defects were more abundant in the 45° and 90° build-up orientations than in the 0° samples, leading to worse corrosion resistance properties. This is particularly evident in the S45 CPP curves, which were characterized by the lowest E_{br} and the highest frequency of metastable pitting events (Figure 6b), so frequent that a passive trait was sometimes difficult to observe, rather than the other build-up orientations of the solution-annealed samples (S0 and S90). The S90 exhibited an imperfect passivity region due to low repassivating properties, even though the E_{rep} was higher and metastable pitting events were less frequent than those observed in the S45 (Figure 6).

The OCP of the BMD samples was monitored for 96 h in a neutral sodium chloride electrolyte to assess the stability of the passive film and its susceptibility to localized corrosion over time [16,17]. The results obtained from the numeric routine applied to the OCP curves are shown in Figure 9, in which only the most representative curve for each sample is plotted for brevity.

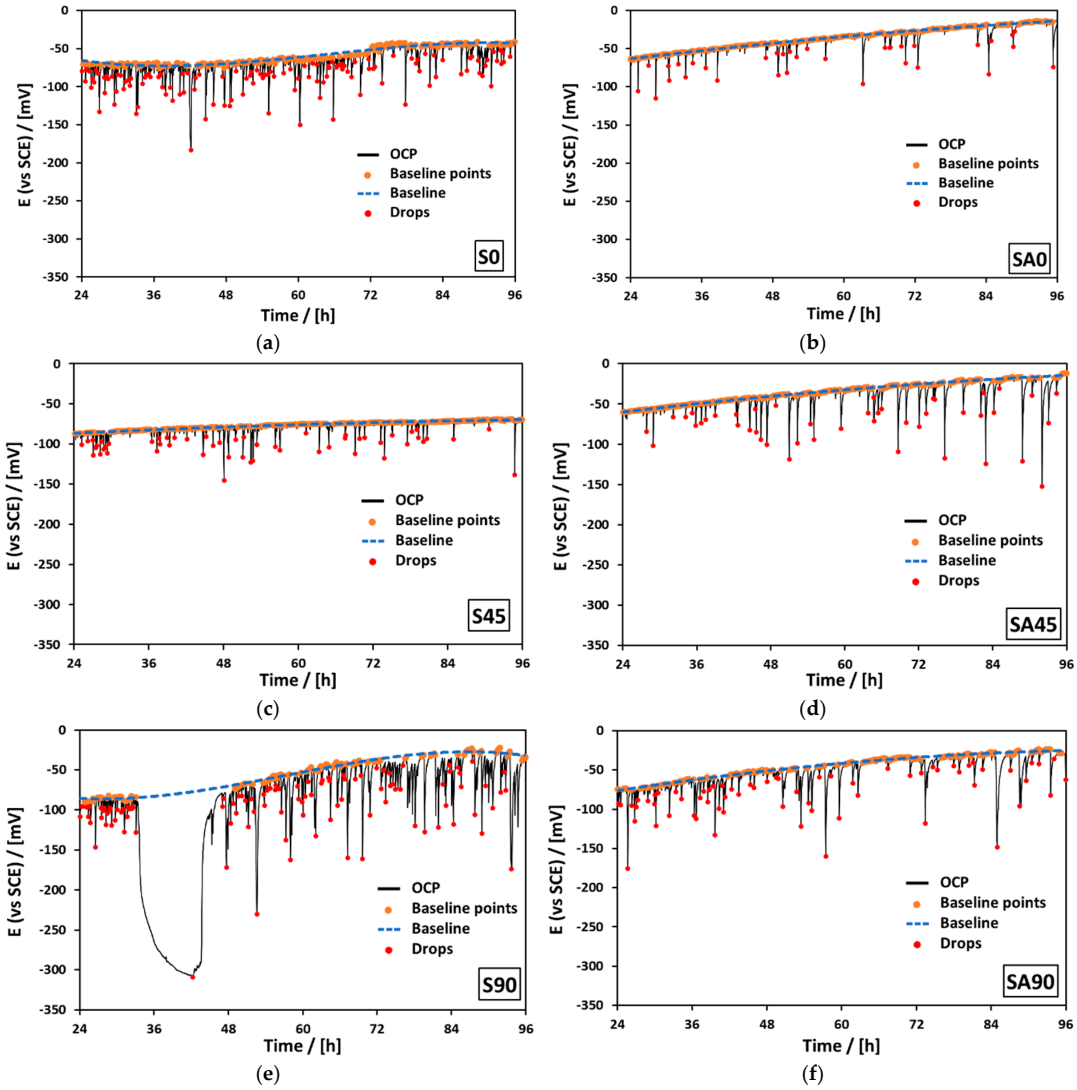

Figure 9. OCP monitoring between 24 h and 96 h analyzed through numeric routine, showing the OCP value (black line), the points used for the polynomial equation of the baseline (orange points), the baseline (blue dashed line), and the minimum of the potential drops (red points) for each sample: S0 (**a**), SA0 (**b**), S45 (**c**), SA45 (**d**), S90 (**e**), and SA90 (**f**).

Although many activation events of the passive film, or potential drops, can be observed in the OCP curves, particularly in the solution-annealed samples, their frequency cannot be considered very representative of the instability of the passive film in a neutral chloride environment. The magnitude of these activation events, or the area of the drops calculated using the trapezoidal rule and expressed by [V·h], has proven more relevant to this investigation. In this context, the significant activation event in the S90 OCP curve occurring between 33 h and 47 h (Figure 9e) cannot be compared to any other throughout the entire exposure in the neutral chloride solution, demonstrating that frequency is not a reliable indicator of the instability of the passive film, but rather the magnitude. Such long-lasting potential drops were not observed in the SA90, indicating that the H900 aging treatment improved the corrosion resistance properties of the passive film. The activation events of the passive films of the other samples lasted less than 30 min and never exceeded −200 mV. No consistent evidence of corrosion was detected following the monitoring of the OCP.

Figure 10 shows the average values and the standard deviations of the summed areas of activation events for the heat-treated samples fabricated by BMD.

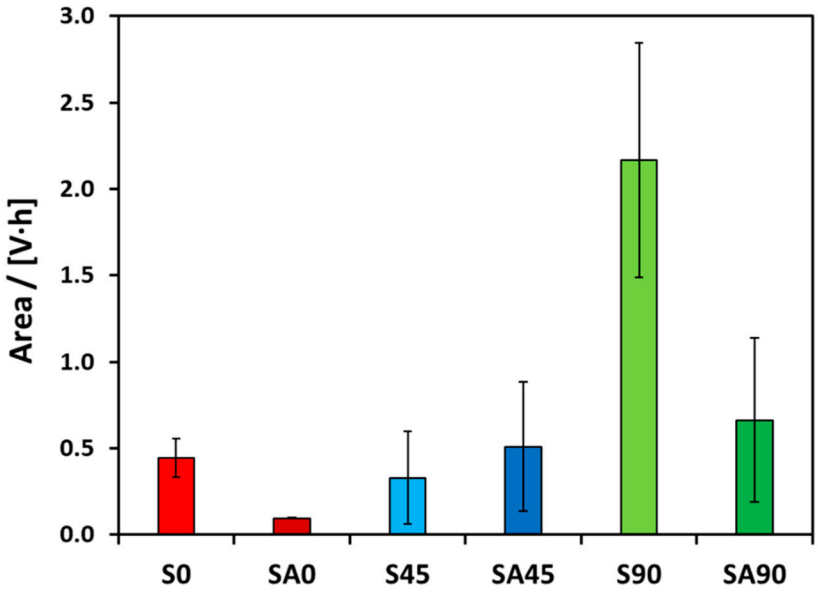

Figure 10. Average values and standard deviations of the summed areas of potential drops for each build-up orientation and heat treatment of the samples fabricated using BMD technology.

The instability of the passive films of the solution-annealed samples was significantly lower than that of the as-sintered reported in similar studies [16,17]. This finding confirms a considerable improvement in the localized corrosion resistance properties after solution annealing heat treatment, as observed in the CPP curves (Figures 6 and 7) and the evaluation of characteristic potentials (Figure 8). In greater detail, the average area of the potential drops for the as-sintered 0° sample was 0.96 V·h, as previously reported [16], which is significantly higher than that of the S0 samples (0.44 V·h). This improvement was even more evident when comparing the as-sintered 90° sample, where the OCP curve showed an active-like behavior from the onset of monitoring [16], with the S90 sample showing a passive-like behavior with many drops. However, solution annealing did not yield significant improvements in the S45 samples, as the average area was comparable to the as-sintered 45° sample [16]. The H900 aging heat treatment performed after solution annealing further decreased the passive film instability of the BMD samples, particularly for the 0°

and 90° build-up orientations, confirming the trends observed in the CPP curves (Figure 7) and characteristic potentials (Figure 8).

However, none of the heat-treated BMD samples achieved an average area comparable to a wrought 17-4 PH, reported to be 0.01 V·h in a similar study [16]. Among the heat-treated BMD samples, the SA0 sample exhibited the lowest instability of the passive film, with an average area of approximately ten times higher (0.10 V·h) than that of a wrought.

As a final consideration of this investigation, the authors emphasize that the analysis of the activation events represents the magnitude of the active tendency of the surfaces of the samples. Although the average areas obtained from the analysis of the drops of the OCP curves (Figure 10) proved reliable for assessing the instability of the passive film in a neutral chloride environment, it may not correlate well with the characteristic potentials obtained from the CPP curves (Figure 8), which represents a good indicator of the corrosion behavior for a short time of immersion (minutes or few hours) of the samples in the neutral chloride electrolyte.

4. Conclusions

The effects of solution annealing and subsequent H900 aging treatments on the corrosion resistance properties of 17-4 PH samples additive-manufactured by Material Extrusion (Bound Metal Deposition^{TM}) with 0°, 45°, and 90° build-up orientations were investigated through chemical composition and X-ray diffraction analysis, microstructural characterizations, cyclic potentiodynamic polarization (CPP) curves, and open circuit potential (OCP) monitoring in neutral sodium chloride electrolytes.

The solution annealing increased the corrosion resistance properties of the samples fabricated using Bound Metal Deposition^{TM}. The CPP curves were characterized by the typical passive trait of stainless steel, with characteristic potentials comparable to a wrought 17-PH, and the OCP monitoring showed improved passive film stability. In contrast, previous studies reported that as-sintered samples exhibited anodic traits typical of active metals and higher passive film instability. The improvements of the corrosion resistance properties following solution annealing were attributed to a growth in the chromium-rich ferritic phase (21–22% wt.%) at the grain boundaries of the martensitic matrix and a finer dispersion of the copper precipitates.

The aging heat treatment (H900) following solution annealing further enhanced the chromium-rich ferritic phase growth, improving the localized corrosion resistance properties of the samples fabricated using Bound Metal Deposition^{TM}. The CPP curves showed higher characteristic potentials and the OCP monitoring was characterized by higher passive film stability than solution-annealed samples.

The build-up orientation influenced the passive film properties as well. Samples with a 0° build-up orientation exhibited the highest resistance to localized corrosion, showing high E_{br}, perfect passivity region ($E_{prot} > E_{corr}$), and good passive film stability. The 45° samples showed passive film properties close to 0° but lower characteristic potentials, particularly for E_{prot}, resulting in imperfect passivity ($E_{prot} < E_{corr}$). On the other hand, 90° samples had better characteristic potentials of the CPP but higher instability of the OCP monitoring.

This study demonstrated how multiple factors influence the corrosion resistance properties of stainless steel fabricated using Material Extrusion in neutral sodium chloride environments. Key factors include microstructure, build-up orientation, and heat treatment. Optimizing the build-up orientation and post-processing heat treatment is crucial for obtaining a microstructure capable of reducing the risk of localized corrosion and improving the performance of components fabricated by Material Extrusion.

Author Contributions: Conceptualization, P.F. and T.B.; methodology, P.F. and T.B.; software, P.F. and T.B.; validation, P.F.; formal analysis, P.F. and T.B.; investigation, P.F.; resources, P.F., T.M., M.S. and T.B.; data curation, P.F.; writing—original draft preparation, P.F.; writing—review and editing, P.F., T.M., M.S. and T.B.; visualization, P.F. and T.M.; supervision, M.S. and T.B. All authors have read and agreed to the published version of the manuscript.

Funding: This research received no external funding.

Data Availability Statement: The data required to reproduce these findings cannot be shared, as they are part of ongoing investigations.

Conflicts of Interest: The authors declare no conflicts of interest.

References

1. Sander, G.; Thomas, S.; Cruz, V.; Jurg, M.; Birbilis, N.; Gao, X.; Brameld, M.; Hutchinson, C.R. On The Corrosion and Metastable Pitting Characteristics of 316L Stainless Steel Produced by Selective Laser Melting. *J. Electrochem. Soc.* **2017**, *164*, C250–C257. [CrossRef]
2. Alam, M.K.; Edrisy, A.; Urbanic, J.; Pineault, J. Microhardness and Stress Analysis of Laser-Cladded AISI 420 Martensitic Stainless Steel. *J. Mater. Eng. Perform.* **2017**, *26*, 1076–1084. [CrossRef]
3. DebRoy, T.; Wei, H.L.; Zuback, J.S.; Mukherjee, T.; Elmer, J.W.; Milewski, J.O.; Beese, A.M.; Wilson-Heid, A.; De, A.; Zhang, W. Additive manufacturing of metallic components—Process, structure and properties. *Prog. Mater. Sci.* **2018**, *92*, 112–224. [CrossRef]
4. Murr, L.E. A Metallographic Review of 3D Printing/Additive Manufacturing of Metal and Alloy Products and Components. *Metallogr. Microstruct. Anal.* **2018**, *7*, 103–132. [CrossRef]
5. Chao, Q.; Cruz, V.; Thomas, S.; Birbilis, N.; Collins, P.; Taylor, A.; Hodgson, P.D.; Fabijanic, D. On the enhanced corrosion resistance of a selective laser melted austenitic stainless steel. *Scr. Mater.* **2017**, *141*, 94–98. [CrossRef]
6. Sander, G.; Tan, J.; Balan, P.; Gharbi, O.; Feenstra, D.R.; Singer, L.; Thomas, S.; Kelly, R.G.; Scully, J.R.; Birbilis, N. Corrosion of additively manufactured alloys: A review. *Corrosion* **2018**, *74*, 1318–1350. [CrossRef] [PubMed]
7. Vafadar, A.; Guzzomi, F.; Rassau, A.; Hayward, K. Advances in metal additive manufacturing: A review of common processes, industrial applications, and current challenges. *Appl. Sci.* **2021**, *11*, 1213. [CrossRef]
8. Suwanpreecha, C.; Manonukul, A. A Review on Material Extrusion Additive Manufacturing of Metal and How It Compares with Metal Injection Moulding. *Metals* **2022**, *12*, 429. [CrossRef]
9. Miura, H.; Osada, T.; Itoh, Y. Metal Injection Molding (MIM) Processing. In *Advances in Metallic Biomaterials*; Springer Series in Biomaterials Science and Engineering; Niinomi, M., Narushima, T., Nakai, M., Eds.; Springer: Berlin, Germany, 2015; Volume 4, pp. 27–56.
10. Huang, N.; Cook, O.J.; Argüelles, A.P.; Beese, A.M. Review of Process–Structure–Property Relationships in Metals Fabricated Using Binder Jet Additive Manufacturing. *Metallogr. Microstruct. Anal.* **2023**, *12*, 883–905. [CrossRef]
11. Nurhudan, A.I.; Supriadi, S.; Whulanza, Y.; Saragih, A.S. Additive manufacturing of metallic based on extrusion process: A review. *J. Manuf. Process.* **2021**, *66*, 228–237. [CrossRef]
12. Singh, G.; Missiaen, J.M.; Bouvard, D.; Chaix, J.M. Additive manufacturing of 17–4 PH steel using metal injection molding feedstock: Analysis of 3D extrusion printing, debinding and sintering. *Addit. Manuf.* **2021**, *47*, 102287. [CrossRef]
13. Mostafaei, A.; Elliott, A.M.; Barnes, J.E.; Li, F.; Tan, W.; Cramer, C.L.; Nandwana, P.; Chmielus, M. Binder jet 3D printing—Process parameters, materials, properties, modeling, and challenges. *Prog. Mater. Sci.* **2021**, *119*, 100707. [CrossRef]
14. Ziaee, M.; Crane, N.B. Binder jetting: A review of process, materials, and methods. *Addit. Manuf.* **2019**, *28*, 781–801. [CrossRef]
15. Di Pompeo, V.; Santecchia, E.; Santoni, A.; Sleem, K.; Cabibbo, M.; Spigarelli, S. Microstructure and Defect Analysis of 17-4PH Stainless Steel Fabricated by the Bound Metal Deposition Additive Manufacturing Technology. *Crystals* **2023**, *13*, 1312. [CrossRef]
16. Forcellese, P.; Mancia, T.; Simoncini, M.; Bellezze, T. Investigation on Corrosion Resistance Properties of 17-4 PH Bound Metal Deposition As-Sintered Specimens with Different Build-Up Orientations. *Metals* **2022**, *12*, 588. [CrossRef]
17. Bianchi, I.; Di Pompeo, V.; Mancia, T.; Pieralisi, M.; Vita, A. Environmental impacts assessment of Bound Metal Deposition 3D printing process for stainless steel. *Procedia CIRP* **2022**, *105*, 386–391. [CrossRef]
18. Sartini, M.; Bianchi, I.; Vita, A.; Germani, M.; Mandolini, M. An analytic cost model for bound metal deposition. *Proc. Des. Soc.* **2024**, *4*, 1819–1828. [CrossRef]
19. Forcellese, P.; Belegni, S.; Silvi, A.; Mancia, T.; Simoncini, M.; Bellezze, T. Study of corrosion resistance of 17-4 PH stainless steel as-sintered and heat treated samples manufactured by Bound Metal Deposition. *Int. J. Ital. Assoc. Metall.* **2023**, *114*, 9–14.
20. Wu, Y.; German, R.M.; Blaine, D.; Marx, B.; Schlaefer, C. Effects of residual carbon content on sintering shrinkage, microstructure and mechanical properties of injection molded 17-4 PH stainless steel. *J. Mater. Sci.* **2002**, *37*, 3573–3583. [CrossRef]

21. Wu, Y.; Blaine, D.; Marx, B.; Schlaefer, C.; German, R.M. Sintering densification and microstructural evolution of injection molding grade 17-4 PH stainless steel powder. *Metall. Mater. Trans. A Phys. Metall. Mater. Sci.* **2002**, *33*, 2185–2194. [CrossRef]
22. Huber, D.; Stich, P.; Fischer, A. Heat Treatment of 17–4 PH Stainless Steel Produced by Binder Jet Additive Manufacturing (BJAM) from N2-Atomized Powder. *Prog. Addit. Manuf.* **2022**, *7*, 187–199. [CrossRef]
23. Chen, Z.; Chen, W.; Chen, L.; Zhu, D.; Chen, Q.; Fu, Z. Influence of initial relative densities on the sintering behavior and mechanical behavior of 316 L stainless steel fabricated by binder jet 3D printing. *Mater. Today Commun.* **2022**, *31*, 103369. [CrossRef]
24. Mirzababaei, S.; Paul, B.K.; Pasebani, S. Microstructure-property relationship in binder jet produced and vacuum sintered 316 L. *Addit. Manuf.* **2022**, *53*, 102720. [CrossRef]
25. Lecis, N.; Mariani, M.; Beltrami, R.; Emanuelli, L.; Casati, R.; Vedani, M.; Molinari, A. Effects of process parameters, debinding and sintering on the microstructure of 316L stainless steel produced by binder jetting. *Mater. Sci. Eng. A* **2021**, *828*, 142108. [CrossRef]
26. Chen, W.; Chen, Z.; Chen, L.; Zhu, D.; Fu, Z. Optimization of Printing Parameters to Achieve High-Density 316L Stainless Steel Manufactured by Binder Jet 3D Printing. *J. Mater. Eng. Perform.* **2023**, *32*, 3602–3616. [CrossRef]
27. Chen, L.; Chen, W.; Fu, Z.; Ding, G.; Chen, Z.; Zhu, D. Binder Jet 3D Printing of 316L Stainless Steel: Orthogonal Printing and Sintering Process Optimization. *Adv. Eng. Mater.* **2023**, *25*, 2200641. [CrossRef]
28. Huber, D.; Vogel, L.; Fischer, A. The effects of sintering temperature and hold time on densification, mechanical properties and microstructural characteristics of binder jet 3D printed 17-4 PH stainless steel. *Addit. Manuf.* **2021**, *46*, 102114. [CrossRef]
29. Pellegrini, A.; Lavecchia, F.; Guerra, M.G.; Galantucci, L.M. Influence of aging treatments on 17–4 PH stainless steel parts realized using material extrusion additive manufacturing technologies. *Int. J. Adv. Manuf. Technol.* **2023**, *126*, 163–178. [CrossRef]
30. Lavecchia, F.; Pellegrini, A.; Galantucci, L.M. Comparative study on the properties of 17-4 PH stainless steel parts made by metal fused filament fabrication process and atomic diffusion additive manufacturing. *Rapid Prototyp. J.* **2023**, *29*, 393–407. [CrossRef]
31. Abe, Y.; Kurose, T.; Santos, M.V.A.; Kanaya, Y.; Ishigami, A.; Tanaka, S.; Ito, H. Effect of layer directions on internal structures and tensile properties of 17-4ph stainless steel parts fabricated by fused deposition of metals. *Materials* **2021**, *14*, 243. [CrossRef] [PubMed]
32. Radhakrishnan, J.; Kumar, P.; Gan, S.S.; Bryl, A.; McKinnell, J.; Ramamurty, U. Microstructure and tensile properties of binder jet printed 17–4 precipitation hardened martensitic stainless steel. *Mater. Sci. Eng. A* **2022**, *860*, 144270. [CrossRef]
33. Mancia, T.; Forcellese, P.; Bellezze, T.; Simoncini, M. Effect of build-up orientation angle and printing speed on mechanical properties and micro- and macro-defect formation in 17-4 PH stainless steel components manufactured by Bound Metal Deposition. *Int. J. Adv. Manuf. Technol.* **2024**, *132*, 4285–4295. [CrossRef]
34. Suwanpreecha, C.; Seensattayawong, P.; Vadhanakovint, V.; Manonukul, A. Influence of Specimen Layout on 17-4PH (AISI 630) Alloys Fabricated by Low-Cost Additive Manufacturing. *Metall. Mater. Trans. A Phys. Metall. Mater. Sci.* **2021**, *52*, 1999–2009. [CrossRef]
35. Banas, J.; Mazurkiewicz, A. The effect of copper on passivity and corrosion behaviour of ferritic and ferritic–austenitic stainless steels. *Mater. Sci. Eng. A* **2000**, *277*, 183–191. [CrossRef]
36. Shu, J.; Bi, H.; Li, X.; Xu, Z. The effect of copper and molybdenum on pitting corrosion and stress corrosion cracking behavior of ultra-pure ferritic stainless steels. *Corros. Sci.* **2012**, *57*, 89–98. [CrossRef]

Disclaimer/Publisher's Note: The statements, opinions and data contained in all publications are solely those of the individual author(s) and contributor(s) and not of MDPI and/or the editor(s). MDPI and/or the editor(s) disclaim responsibility for any injury to people or property resulting from any ideas, methods, instructions or products referred to in the content.